Defect compensation by Cr vacancies and oxygen interstitials in Ti^{4+}-doped Cr_2O_3 epitaxial thin films

Tiffany C. Kaspar,[1,*] Peter V. Sushko,[1] Mark E. Bowden,[2] Steve M. Heald,[3] Alexandra Papadogianni,[4] Carsten Tschammer,[4] Oliver Bierwagen,[4] and Scott A. Chambers[1]

[1] *Physical and Computational Sciences Directorate, Pacific Northwest National Laboratory, P.O. Box 999, Richland, Washington 99352, USA*

[2] *Environmental Molecular Sciences Laboratory, Pacific Northwest National Laboratory, P.O. Box 999, Richland, Washington 99352, USA*

[3] *Advanced Photon Source, Argonne National Laboratory, 9700 S Cass Avenue, Argonne, Illinois 60439, USA*

[4] *Paul-Drude-Institut für Festkörperelektronik, Hausvogteiplatz 5–7, D-10117 Berlin, Germany*

(Received 27 July 2016; published 7 October 2016)

Epitaxial thin films of $Cr_{2-x}Ti_xO_3$ were deposited by oxygen-plasma-assisted molecular beam epitaxy for $0.04 \leqslant x \leqslant 0.26$. Ti valence is verified by both x-ray photoelectron spectroscopy (XPS) and Ti K-edge x-ray absorption near-edge spectroscopy (XANES) to be Ti^{4+}. Substitution of Ti for Cr in the corundum lattice is verified by fitting the Ti K-edge extended x-ray absorption fine structure (EXAFS) data. Room temperature electrical transport measurements confirm the highly resistive nature of Ti-doped Cr_2O_3, despite the presence of aliovalent Ti^{4+}. For comparison, the resistivity of very pure, undoped Cr_2O_3 was measured to be four orders of magnitude higher than for Ti-doped Cr_2O_3. Analysis of the XPS and EXAFS data reveal the presence of Cr vacancies at intermediate and high Ti concentrations. This conclusion is corroborated by the results of density functional modeling. At low Ti concentrations, a strong increase of the XPS Ti $2p$ core level peak width is observed as the Ti concentration decreases. In this limit, the formation of Cr vacancies becomes less favorable due to the increased distance between Ti dopants, and compensation by O interstitials contributes to broadening of the Ti $2p$ XPS peak. The differences in electronic structure which render Ti^{4+}-doped Cr_2O_3 resistive due to the formation of compensating defects, but Ti^{4+}-doped Fe_2O_3 conductive, are discussed. The defect compensation model developed here provides insight into previous, conflicting reports of n-type versus p-type conductivity in Ti-doped Cr_2O_3 at high temperature, and will inform future studies to exploit the wide variety of electronic and magnetic properties of corundum structure oxides.

DOI: 10.1103/PhysRevB.94.155409

I. INTRODUCTION

Eskolaite, α-Cr_2O_3, is of interest for applications ranging from corrosion-resistant coatings on metals [1,2] to next-generation photocatalysts for water splitting to generate H_2 [3–5]. Cr_2O_3 is a wide bandgap oxide ($E_g = 3.3$ eV) which adopts the hexagonal corundum crystal structure shared by α-Al_2O_3, Ti_2O_3, α-Fe_2O_3, and V_2O_3. These oxides exhibit rich spin physics and electronic properties, including a metal-insulator transition in V_2O_3 at 155 K [6], a semiconductor-metal transition in Ti_2O_3 at 400–600 K [6], canted antiferromagnetic ordering which persists to 948 K in α-Fe_2O_3 [7], and magnetoelectric coupling of antiferromagnetic α-Cr_2O_3 at room temperature [8]. Isostructural doping with $M =$ Al, Ti, V, Cr, or Fe provides another avenue to tune the properties of the corundum structure oxides.

As one example, Ti-doped Cr_2O_3 has been extensively studied as a gas sensor [9,10]. The solid-state reaction of TiO_2 and Cr_2O_3, and subsequent high-temperature calcination, was found to result in a material which exhibits significant Ti segregation to the surface, as well as some Cr^{6+} in the surface region [10,11]. Deposition of nanostructured thin films by electrostatic spray-assisted vapor deposition [12] or atmospheric pressure chemical vapor deposition [13] at lower temperatures (450–650 °C) also resulted in Ti surface segregation. Nonetheless, $Cr_{1.8}Ti_{0.2}O_3$ exhibits superior gas-sensing properties, which makes it suitable for commercial gas sensors [11].

Substitutional Ti in the Cr_2O_3 lattice is assumed to take the +4 valence state, with the formation of compensating Cr vacancies to maintain charge neutrality [10,11]. The response of the material to oxidizing and reducing gases implies that the electrical conductivity is p-type [11]. This is in contrast to the expectation that p-type conductivity results from doping with lower valence metals, as is observed for Mg^{2+}-doped Cr_2O_3 [14], while n-type conductivity results when doping with higher valence metals such as Ti^{4+}, as occurs in the isostructural Ti-doped Fe_2O_3 system. Pristine Fe_2O_3 exhibits rather poor transport characteristics dominated by small polaron hopping in the Fe^{3+} bilayers [15]. Substitutional doping with Ti has been found to strongly increase the free electron carrier concentration and mobility [16,17]. A previous paper by our group [18] showed that, for epitaxial thin films deposited by oxygen-plasma-assisted molecular beam epitaxy (OPA-MBE), Ti substituted in the Fe_2O_3 lattice as Ti^{4+} (not Ti^{3+}, as would be expected from analogy to isostructural Ti_2O_3) and relatively low Ti concentrations of $y < 0.10$ in $(Ti_yFe_{1-y})_2O_3$ were sufficient to increase the n-type carrier concentration to the 10^{19} cm^{-3} range. The n-type carriers arise from the substitutional Ti_{Fe}, which donate electrons to the Fe_2O_3 conduction band under relatively oxygen-poor deposition conditions; the conduction mechanism was found to be small polaron hopping at room temperature, transitioning to variable

*tiffany.kaspar@pnnl.gov

 ©2016 American Physical Society

range hopping at lower temperatures. Under oxygen-rich conditions, it was hypothesized that Fe vacancies ($V_{\rm Fe}'''$) form as the primary defect compensation mechanism, rendering the material insulating. The n-type carrier concentration is thus governed by [18]:

$$n - p = [\mathrm{Ti}_{\mathrm{Fe}}^{\bullet}] - 3[V_{\mathrm{Fe}}'''] \quad (1)$$

where n and p are the concentrations of free electrons and holes, respectively, and $[\mathrm{Ti}_{\mathrm{Fe}}^{\bullet}]$ is the concentration of substitutional Ti^{4+}. The defect concentrations are determined primarily by the oxygen fugacity during deposition [19].

Fundamental studies of bulk Ti-doped Cr_2O_3 have been undertaken in an attempt to clarify the defect compensation mechanism and transport properties. Holt and Kofstad [20] made a careful study of the high-temperature transport properties of Cr_2O_3 doped with 2mol% TiO_2($Cr_{1.98}Ti_{0.02}O_3$) as a function of oxygen activity (proportional to the partial pressure of O_2 in equilibrium with the specimen). At lower temperatures (440 °C to ∼1000 °C), the transport characteristics of Cr_2O_3 were dominated by unintentional extrinsic impurities, such as Mg^{2+}, and thus the intrinsic transport characteristics of Cr_2O_3 (and Ti-doped Cr_2O_3) could not be established [21]. At 1000 °C, they observed weak conductivity and a crossover in the transport characteristics of $Cr_{1.98}Ti_{0.02}O_3$ from n-type at low oxygen activity to p-type at high oxygen activity. The defect model which Holt and Kofstad proposed to rationalize this behavior assumes that a reservoir of TiO_2, representing Ti which has not dissolved in the Cr_2O_3 lattice, forms and equilibrates with substitutional Ti at a given oxygen activity. However, Atkinson *et al.* [22] found that, for the same temperature of 1000°C and similar variation in oxygen activity, a higher Ti doping level ($Cr_{1.7}Ti_{0.3}O_3$) resulted in monotonically increasing n-type conductivity as the oxygen activity was decreased; no indications of p-type transport were observed. Bulk density measurements implied the presence of compensating Cr vacancies, and density functional theory (DFT) calculations suggested the formation of neutral defect complexes consisting of three substitutional Ti^{4+} and a neighboring Cr vacancy. The observed n-type conduction was thought to arise from a small concentration of Ti^{4+} which is not associated with a vacancy complex and thus donates electrons to the conduction band.

In contrast to the results for bulk Ti-doped Cr_2O_3, a textured thin film study [23] claimed Ti^{3+} substitution for Cr^{3+} on the basis of x-ray photoelectron spectroscopy (XPS) measurements; however, the carrier type could not be determined by Hall measurements due to high sample resistivity, even at elevated temperatures (500 K). Nonetheless, *ex situ* Ti diffusion into these textured films was found to increase the n-type carrier concentration, which was attributed to the incorporation of Ti^{4+} [24]. This is supported by a recent DFT study, which predicted Ti substitution as Ti^{4+} with a free electron in the conduction band [25].

Clearly, fundamental questions about Ti-doped Cr_2O_3 remain: Does Ti substitution lead to n-type or p-type carrier doping? What defect compensation mechanism(s) render Ti-doped Cr_2O_3 highly resistive, even at higher Ti concentrations? What properties govern the different transport behavior observed for Ti-doped Cr_2O_3 compared with Ti-doped Fe_2O_3? Well-defined and well-characterized samples in which Ti is shown to substitute in the corundum lattice are required to clarify the intrinsic properties of Ti-doped Cr_2O_3 in the absence of extrinsic impurities, grain boundaries, secondary phases, and dopant segregation. This has been accomplished in the present paper by depositing epitaxial thin films of $Cr_{2-x}Ti_xO_3$ of ultra-high purity. Thorough materials characterization, electrical transport measurements, and modeling combine to elucidate the intrinsic properties of Ti-doped Cr_2O_3.

II. EXPERIMENTAL METHODS

Epitaxial thin films of $Cr_{2-x}Ti_xO_3$ ($0.04 < x < 0.26$) were deposited on α-Al_2O_3(0001) single crystal substrates by OPA-MBE. Substrate surfaces were precleaned *in situ* by exposure to activated oxygen from an electron cyclotron resonance (ECR) microwave plasma source at room temperature and a background oxygen pressure of 2×10^{-5} Torr for 30 min. The flow of activated oxygen was maintained as the substrate was heated to the deposition temperature of 550 °C ($x \leqslant 0.05$) or 700–750 °C ($x > 0.05$) and, under typical growth conditions, continued during the deposition. To explore the effect of oxygen activity on the defect structure of the films, some depositions were performed without the oxygen plasma in an O_2 partial pressure between 2×10^{-5} and 8×10^{-7} Torr. Cr metal (99.995% pure) was evaporated from an electron beam evaporator, and the flux was monitored by atomic absorption spectroscopy. Ti metal (99.99% pure) was sublimed from an effusion cell fitted with a proprietary Ti-compatible crucible (DCA Instruments Inc.). The overall growth rate was 0.24 Å/s to a final film thickness of 500 Å. For higher Ti concentrations ($x > 0.08$), the deposition of a 50 Å pure Cr_2O_3 buffer layer was required to establish epitaxy before Ti was introduced. To avoid overoxidation of Cr on the film surface [26,27] after Ti-doped Cr_2O_3 film deposition, the plasma source was switched off at the end of the growth and the O_2 flow immediately ceased before the substrate temperature was decreased. Structural quality and morphology were monitored *in situ* before, during, and after deposition with reflection high-energy electron diffraction (RHEED).

High-energy resolution XPS data were collected *in situ* in an appended ultra-high vacuum chamber utilizing a monochromated Al K_α x-ray source ($\lambda = 1486.6$ eV) and a Gamma-Data/Scienta SES-200 hemispherical analyzer. The energy resolution of the SES-200 spectrometer is approximately 0.5 eV for the photoemission spectra reported here. A low-energy electron flood gun was utilized to compensate for charging effects in these highly resistive materials. High-resolution spectra were placed on an absolute binding energy (BE) scale by shifting the O1s peak to align at 530.0 eV [28]. *Ex situ* x-ray diffraction (XRD) patterns and reciprocal space maps were collected on a Philips X'Pert Materials Research Diffractometer (MRD) using Cu$K_{\alpha 1}$ radiation monochromated with a hybrid mirror/four-crystal monochromator. High-resolution θ–2θ scans and reciprocal space maps were collected with fixed-slit detector optics. Ellipsometry data were collected as a function of incident photon energy with a variable-angle spectroscopic ellipsometer (V-VASE, J.A. Woollam) at angles of 50°, 60°, and 70°. Data were fit using the WVASE software program.

Charge states and local structure were determined by Cr and Ti K-edge x-ray absorption near-edge spectroscopy (XANES) and extended x-ray absorption fine structure (EXAFS) on the PNC/XSD beamline 20-BM at the Advanced Photon Source (Argonne, Illinois). Measurements were made in fluorescence mode at glancing angles ($\sim 5^\circ$ incident angle), with the x-ray polarization both perpendicular (perp) and parallel (par) to the surface. Si (111) monochromator crystals were used with slit settings small enough that the energy resolution is dominated by the Si(111) crystals ($\Delta E/E = 1.4 \times 10^{-3}$). EXAFS data were quantitatively analyzed with the fitting program Artemis (version 0.8.012) by fitting par and perp data simultaneously for each film with a k range from $k = 2$ Å^{-1} to $k = 9$–12 Å^{-1}, depending on the noise level of the data. The scattering path data calculated by FEFF6 utilized the POLARIZATION card to account for the polarization with respect to the crystal orientation. Single-scattering paths out to second cation and anion neighbors were typically included in the fit. Scattering distances and Debye-Waller factors were unconstrained, but the coordination numbers were fixed at the ideal lattice values. This resulted in 9–10 independent fit variables (depending on whether the amplitude factor S_0^2 was varied or fixed, as discussed below).

Resistivity measurements were performed on transmission line measurement (TLM) devices consisting of five contacts, with various spacings ranging from 2 to 20 μm and a length of 1 mm, which were deposited *ex situ* on selected pure and Ti-doped Cr_2O_3 films. Additionally, interdigitated contact patterns with spacings of 20 μm (25 contract pairs, length of 780 μm) and 7 μm (71 contact pairs, length of 780 μm) were also utilized, which can reduce the measured two-terminal resistance with respect to the sheet resistance by a factor of roughly 10^{-3} and 10^{-4}, respectively. The metal stacks of all structures consisted of a 150-nm layer of Au on top of a 20-nm layer of Ti and were deposited by electron beam evaporation. Two-terminal resistance measurements using these structures were performed on approximately 1×1-cm^2 samples in the ambient environment. Due to the highly resistive nature of the films, and possibly very low mobility, Hall effect measurements were unsuccessful. Likewise, the van der Pauw method did not provide reliable sheet resistance measurements.

DFT modeling was performed using the Vienna *Ab initio* Simulation Package (VASP) [29]. The projector-augmented wave (PAW) method [9] was used to approximate the electron-ion potential, and exchange-correlation effects were treated within the generalized gradient approximation (GGA) and Perdew-Burke-Ernzerhof (PBE) functional form [30] modified for solids (PBEsol) [31]. The $4 \times 4 \times 4$ Monkhorst-Pack k-point mesh was used for static energy minimization and calculations of the densities of states. To mitigate the well-known deficiencies of GGA in describing band gaps and defect electronic states, we adopted the GGA+U approach [32] and fitted the value of U, applied to $3d$ states only. We considered the range of U_{Cr} from 2.0 to 4.4 eV. $U_{\mathrm{Cr}} = 3.9$ eV was found to provide the best compromise of lattice parameters and electronic structure. The lattice and electronic structure dependence on U_{Ti} is discussed in detail below. The thermodynamic stability of various $Cr_{2-x-y}Ti_xO_3$ and $Cr_{2-x}Ti_xO_{3+z}$ phases, containing substitutional Ti_{Cr} and either Cr vacancies (V_{Cr}) or interstitial oxygen species (O_i), were calculated with respect to the uncompensated phases $Cr_{2-x}Ti_xO_3$ and pure α-Cr_2O_3 following an approach described elsewhere [33]. The calculations were performed using the orthorhombic $Cr_{24}O_{36}$ supercell. In the case of Ti_{Cr} dopants and $Ti_{\mathrm{Cr}} + V_{\mathrm{Cr}}$ defect complexes, all non-equivalent configurations were considered. In the case of $Ti_{\mathrm{Cr}} + O_i$ defect complexes, we considered several configurations corresponding different distances between Ti_{Cr} and O_i. In each case the total energy was minimized with respect to the internal coordinates and lattice parameters.

III. RESULTS

A. Epitaxy and film structure

The epitaxial deposition of α-Cr_2O_3 [26,34], α-Fe_2O_3 [35–39], $(Fe,Cr)_2O_3$ [40], and $(Fe,Ti)_2O_3$ [16,18] thin films on α-$Al_2O_3(0001)$ substrates by OPA-MBE is well established. Despite the significant lattice mismatch between Cr_2O_3 ($a = 4.96$ Å) and Al_2O_3 ($a = 4.76$ Å) of $\delta = (a_{Cr_2O_3} - a_{Al_2O_3})/a_{Al_2O_3} = 4.2\%$, thin layers of Cr_2O_3 grow well with a smooth surface, and for that reason, Cr_2O_3 has been used to grade the lattice mismatch between Al_2O_3 and Fe_2O_3 ($a = 5.04$ Å) [41]. The deposition of Ti-doped Cr_2O_3 on $Al_2O_3(0001)$ is expected to behave very similarly to the deposition of pure Cr_2O_3, since the ionic radius of Ti^{4+} (0.605 Å) is very similar to that of Cr^{3+}(0.615 Å), and thus a negligible change in the lattice parameter occurs upon substitutional doping [22]. Indeed, $Cr_{2-x}Ti_xO_3$ films are epitaxial and crystalline for $x \leqslant 0.05$. Surprisingly, however, for $x > 0.08$ the deposition of $Cr_{2-x}Ti_xO_3$ on Al_2O_3 resulted in amorphous films (as judged by the loss of RHEED diffraction features). Epitaxy was only realized if a thin (50 Å) Cr_2O_3 buffer layer was deposited before the introduction of Ti. As shown by the XRD and RHEED patterns in Fig. 1(a), with the inclusion of this buffer layer, the Ti-doped Cr_2O_3 film exhibits epitaxy, even at a high dopant concentration of $x = 0.26$. Finite-thickness interference fringes are observed in the XRD θ–2θ scan, indicating that the film is well-ordered in the out-of-plane direction, with a sharp interface at the substrate. The asymmetry of the (006) film reflection, and marked asymmetry of the finite thickness fringes, arises in part from interference of the pure Cr_2O_3 buffer layer. Nonuniform strain fields in the film, due to incomplete relaxation of epitaxial strain, may also contribute to this asymmetry. The surface morphology can also be inferred from the RHEED patterns: slight modulation of the streaks is observed, indicating some surface roughness.

A reciprocal space map (RSM) of the (1 0 10) reflection of the film and substrate is presented in Fig. 1(b). The elongation of the substrate reflection is an artifact of the x-ray optics employed during the measurement. The reflection from the $Cr_{1.72}Ti_{0.26}O_3$ film appears as a single peak, confirming an in-plane epitaxial relationship with the substrate. Despite the large lattice mismatch, the peak does not lie at the fully relaxed (bulk-like) position. Additionally, the reflection is broadened in the in-plane (q_{xy}) direction, consistent with the broad (006) reflection in Fig. 1(a). Again this likely represents a range of strain states in the film. In agreement with previous reports [23], a weak trend of an increasing c lattice parameter and decreasing a lattice parameter was observed with increasing

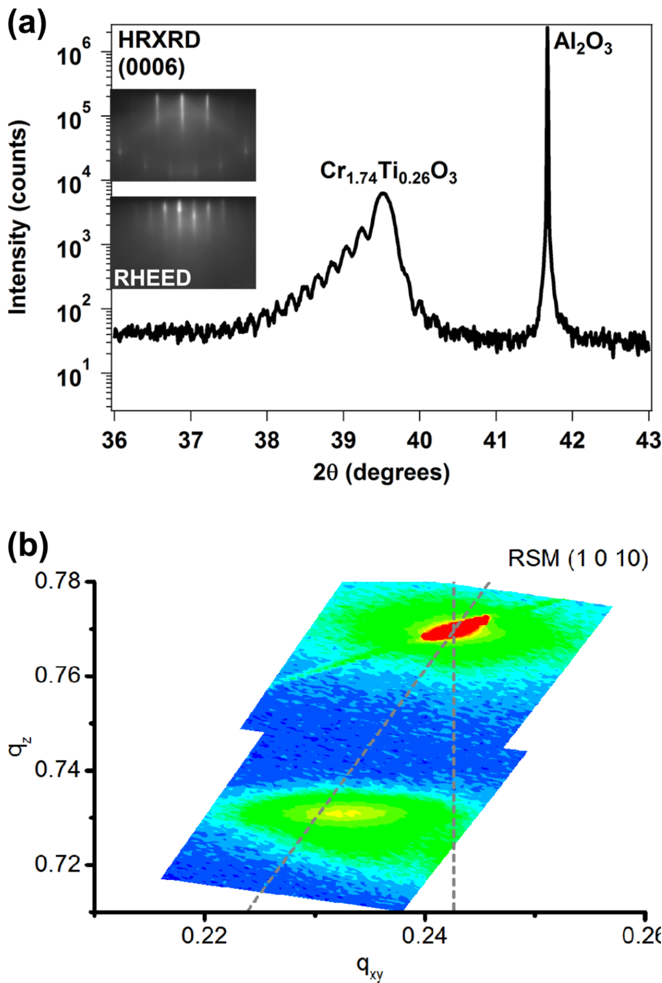

FIG. 1. X-ray diffraction patterns of $Cr_{1.74}Ti_{0.26}O_3$. (a) Out-of-plane θ–2θ pattern. Inset shows *in situ* RHEED patterns after deposition. (b) Reciprocal space map (RSM) of the (1 0 10) reflection of the α-Al_2O_3 substrate (top) and film (bottom). Dashed lines indicate relationship between film and substrate peaks assuming coherent epitaxial growth (vertical) or fully relaxed film (diagonal).

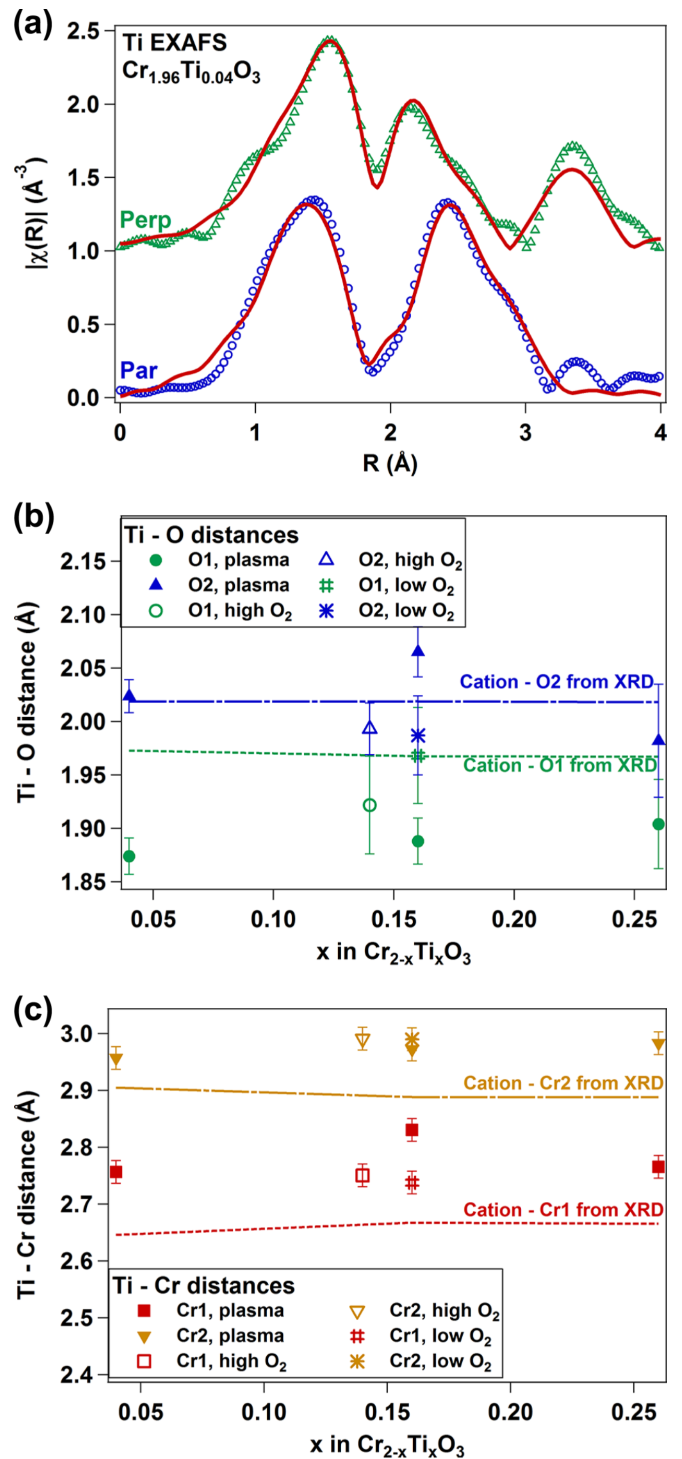

FIG. 2. (a) Ti K-edge EXAFS data (symbols) and fits (solid lines) for $Cr_{1.96}Ti_{0.04}O_3$. (b) First shell Ti–O distances (symbols) from EXAFS fits to films deposited with the oxygen plasma and films deposited in O_2. Dashed and dash-dot lines indicate the expected distances determined from the XRD lattice parameters. (c) Second shell Ti-Cr distances from the same EXAFS fits (symbols) and XRD lattice parameters (dashed and dash-dot lines).

Ti doping concentration from $c = 13.569$ to 13.670 Å and $a = 4.987$ to 4.957 Å for $x = 0.04$ to 0.26. However, we attribute this trend to incomplete strain relaxation, not an intrinsic change in the lattice parameters of Ti-doped Cr_2O_3, as evidenced by the lattice parameters measured for a thick (4900 Å) film of $Cr_{1.80}Ti_{0.20}O_3$: c = 13.593 Å and $a =$ 5.005 Å. For reference, the lattice parameters of bulk Cr_2O_3 are generally taken as $c = 13.599$ Å and $a = 4.9607$ Å [7].

Analysis of the Ti and Cr K-edge EXAFS data confirms Ti substitution in the corundum lattice. Figure 2(a) presents the Ti K-edge EXAFS Fourier transformed $\chi(R)$ spectra for $Cr_{1.96}Ti_{0.04}O_3$. The local environment around Cr in pure Cr_2O_3 is affected by both misfit dislocations that form to relieve the epitaxial strain to the substrate and, if this strain relaxation is incomplete, as indicated by the XRD patterns in Fig. 1, residual strain fields. In the Ti-doped films, the additional presence of charge-compensating point defects reduces the fit quality, with strong correlation between fit parameters, of the pseudo-radial distribution function (RDF) for all Ti concentrations investigated. In particular, the amplitude factor (S_0^2) is primarily a function of the emitting element and thus is expected to remain approximately the same value across all fits. An unconstrained fit to the $Cr_{1.96}Ti_{0.04}O_3$ film [shown in

Fig. 2(a)], which presumably possesses less disorder than the films with higher Ti concentrations, resulted in an S_0^2 value of 0.7; likewise, a fit to the Cr K-edge RDF for the same film produced a similar S_0^2 value of 0.65. However, S_0^2 was found to increase significantly with increasing Ti concentration, rising as high as 1.049 for a similar unconstrained fit to $Cr_{1.74}Ti_{0.26}O_3$. To keep the fits consistent between films, the amplitude factor was constrained to a value of 0.7 for all Ti K-edge EXAFS fits. Despite the difficulty in obtaining high-quality fits, it is clear from the Ti K-edge RDF in Fig. 2(a) that Ti is substitutional in the corundum lattice. No evidence of a secondary phase such as rutile or anatase TiO_2 is observed, even for higher Ti concentrations.

In the corundum lattice, the cations are six-fold coordinated, bonding to O ions in a distorted octahedral environment [42]. The unstrained Cr_2O_3 structure consists of three Cr-O bonds at 1.964 Å and three at 2.013 Å. An analysis of the Ti-O nearest-neighbor (NN) distances from the EXAFS fits is plotted in Fig. 2(b), along with the predicted values determined using the lattice parameters measured by XRD (which, as discussed above, are reasonably close to the ideal values, since the Ti-doped Cr_2O_3 films are nearly fully relaxed). Greater distortion is observed for the Ti octahedra than predicted from the bulk crystal structure. Most notably, the closest Ti-O NN distances (Ti–O1) are significantly shorter than expected, although the longer Ti–O2 distances show no clear trend with regard to the predicted values. These Ti–O distances can be compared with those for TiO_2 in the anatase and rutile polymorphs: in anatase, Ti–O1 = 1.937 Å and Ti–O2 = 1.966 Å, and in rutile Ti–O1 = 1.946 Å and Ti–O2 = 1.983 Å. For both polymorphs, the Ti–O1 distances are shorter than those found in ideal Cr_2O_3, but longer than those determined by EXAFS fitting in Fig. 2(b). A similar distortion in the Ti–O octahedra is observed for $Ti_{0.14}Cr_{0.86}O_3$ deposited in 8×10^{-6} Torr O_2 without activated oxygen from the plasma, but the distortion disappears entirely for $Ti_{0.16}Cr_{0.84}O_3$ deposited in 8×10^{-7} Torr O_2 without activated oxygen. In this case, the identical Ti–O1 and Ti–O2 distances found from the EXAFS fit likely indicates a significant amount of crystalline disorder in this film, consistent with the modulated RHEED pattern (not shown), which revealed surface roughness. The next nearest-neighbor (NNN) Ti–Cr distances plotted in Fig. 2(c) show consistent expansion relative to the ideal values for films deposited under all conditions.

In a previous EXAFS study of Ti-doped Cr_2O_3 powder material, Blacklocks *et al.* [43] also obtained poor-quality fits to their data, which they attributed to significant structural disorder. In that paper, the NN Ti–O1 and Ti–O2 distances refined to the same value, indicating that the octahedral distortion had been lifted, in contrast to the results in Fig. 2(b). However, the Ti–O distance from their fits was contracted, with values of 1.937–1.957 Å depending on Ti concentration, which is qualitatively similar to the contracted Ti–O1 distances in Fig. 2(b). The NNN Ti–Cr distances in the powder material were slightly expanded, consistent with the results for the epitaxial films shown in Fig. 2(c). This NNN expansion is consistent with DFT calculations [25], but the contraction in the NN Ti–O distances was not predicted (instead, simulations predicted an expansion in the NN shell, as well as the outer shells). The NN Ti–O contraction may be related to the defects that form to maintain charge neutrality and will be discussed in detail below.

B. Electronic structure and Ti valence

To understand the defect compensation mechanisms and electrical transport properties of Ti-doped Cr_2O_3, it is necessary to first determine the electronic structure of the material and the Ti dopant valence. To this end, *in situ* core level XPS results are presented in Fig. 3. The O1s and Cr 2p core level peaks in Figs. 3(a) and 3(b), respectively, exhibit some broadening when doped with Ti; the Cr 2p peaks show an approximately 0.2 eV increase in full width at half maximum (FWHM) compared with pure Cr_2O_3, while the FWHM of the O1s peaks broaden somewhat more (ΔFWHM ≈ 0.4 eV) when Ti is doped into Cr_2O_3. Slight changes in broadening are observed at different Ti concentrations for both the O1s and Cr 2p peaks. These changes do not follow a monotonic dependence on Ti concentration and instead are attributed to slight changes in the effectiveness of external charge compensation between samples. As shown in Fig. 3(c), however, more dramatic changes are observed in the Ti 2p spectra. To illustrate these changes, Fig. 3(c) also plots the Ti 2p spectrum from slow-grown $Fe_{1.92}Ti_{0.08}O_3$, which is known to exhibit substitutional Ti^{4+} in the Fe_2O_3 lattice and electrically insulating behavior [18]. This spectrum exhibits a slight broadening (FWHM = 1.31 eV) compared with the spectrum for Ti^{4+} in a well-defined crystal lattice such as $SrTiO_3$ (FWHM = 1.07 eV) [44]. In contrast, the Ti 2p core level peaks for the Ti-doped Cr_2O_3 films exhibit substantial broadening, which scales inversely with the Ti concentration; for $Cr_{1.96}Ti_{0.04}O_3$, the FWHM is 2.65 eV. Although the peak narrows somewhat with increasing Ti concentration, as shown in the inset to Fig. 3(c), it does not approach the FWHM value for Ti-doped Fe_2O_3. In addition to the peak broadening, the inset to Fig. 3(c) shows that the position of the Ti $2p_{3/2}$ peak centroid (defined as the center of intensity at half maximum) shifts to higher BE as the Ti concentration decreases from $x = 0.05$ to $x = 0.026$; for $x > 0.05$ the peak position remains within 458.0–458.1 eV. The nominal position of Ti^{4+} in rutile TiO_2 is 458.8 eV [45], well above the centroid positions of all the Ti 2p spectra from Ti-doped Cr_2O_3 films shown in Fig. 3(c). As shown in Fig. 3(d), the broad Ti 2p spectrum for $Cr_{1.84}Ti_{0.16}O_3$ can be fit with two Voigt peaks separated by $\sim$1.0 eV. The best fit position for the Voigt peak at higher BE is found to be 458.6 eV, close to the nominal position for Ti^{4+} in $SrTiO_3$. However, the separation between the two Voigt peaks, $\sim$1.0 eV, is less than the separation between Ti^{4+} and Ti^{3+}, which is typically found to be in the range of 1.5–2.0 eV [45–47]. Similar Ti 2p peak shifts and broadening were observed previously in Ti-doped Cr_2O_3 powder material [10] and assigned as substitutional Ti^{4+}, with the BE shift and peak broadening attributed to screening and local differences in the charging or lattice environment around the Ti^{4+} ions, respectively. In contrast, a textured thin film study [23] attributed similar peak shifting and broadening to the incorporation of substitutional Ti^{3+} in the Cr_2O_3 lattice.

To better elucidate the valence state of substitutional Ti in Cr_2O_3, Ti K-edge XANES spectra are presented in Fig. 4. Comparison of the absorption edge position of the Ti-doped

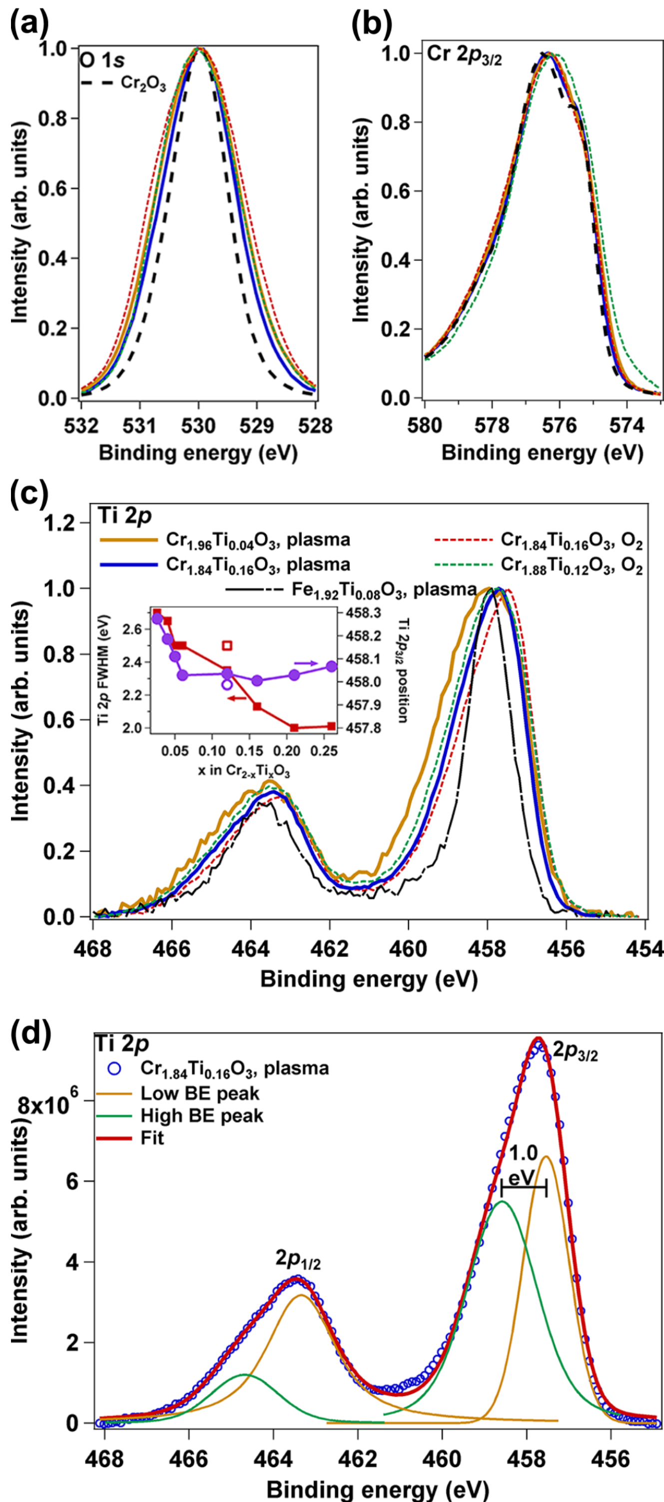

FIG. 3. *In situ* high-resolution XPS spectra of (a) O 1s, (b) Cr 2$p_{3/2}$, and (c) Ti 2p core level spectra. All spectra are referenced to O1s at 530.0 eV. Inset to panel (c) plots the Ti 2$p_{3/2}$ FWHM (left axis) and centroid position (right axis) as a function of Ti concentration for films deposited with the oxygen plasma (filled symbols) and in O_2 (open symbols). The same line colors and styles for each sample are used in parts (a), (b), and (c). (d) Fit of $Cr_{1.84}Ti_{0.16}O_3$ to two components at high and low BE, respectively.

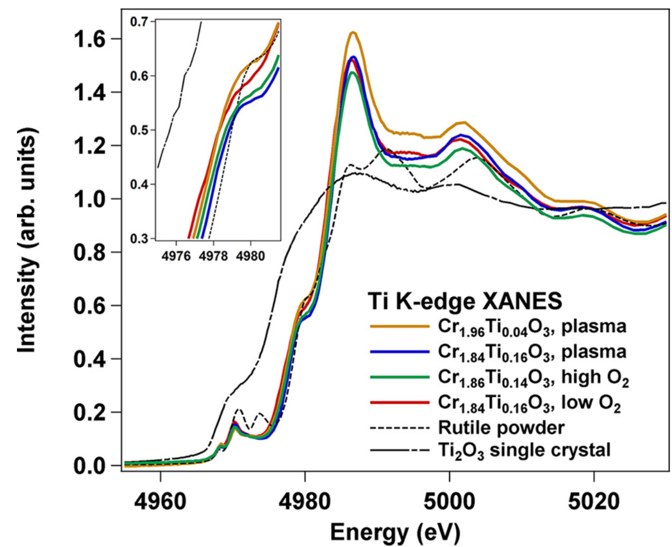

FIG. 4. Ti K-edge XANES spectra (perp polarization) of Ti-doped Cr_2O_3 films, as well as reference standards of TiO_2 rutile powder (Ti^{4+}) and a synthetic Ti_2O_3 single crystal (Ti^{3+}). "High O_2" refers to 8×10^{-6} Torr O_2, and "low O_2" corresponds to 8×10^{-7} Torr O_2. Inset expands the absorption edge region.

Cr_2O_3 films with reference spectra for rutile TiO_2 powder and a synthetic Ti_2O_3 single crystal (synthesized at Lincoln Laboratory [48] and measured along with the Ti-doped Cr_2O_3 films in this paper) indicates that the Ti valence state in the films is nominally Ti^{4+}. Closer inspection of the leading edge (inset to Fig. 4) reveals only minor variations in position. Both $Cr_{1.84}Ti_{0.16}O_3$ deposited in O_2 and $Cr_{1.96}Ti_{0.04}O_3$ exhibit a slight edge shift to lower energy, indicating that they may contain a small fraction of Ti^{3+} (<20% of the total Ti present). Nonetheless, the XANES data confirms that Ti substitutes primarily as Ti^{4+} in the Cr_2O_3 lattice. Thus, the broad Ti 2p peaks and centroid shifts observed by XPS for all Ti-doped Cr_2O_3 films arise from substitutional Ti^{4+}, without a significant Ti^{3+} component.

The electronic structure changes that occur with Ti^{4+} substitution in the Cr_2O_3 lattice were explored with spectroscopic ellipsometry. Figure 5(a) plots the index of refraction, n, and extinction coefficient, k, for thick epitaxial films of both pure Cr_2O_3 (4400 Å thick) and $Cr_{1.80}Ti_{0.20}O_3$ (4900 Å thick). Despite the relatively low Ti doping level, significant changes are seen in the fine structure of both n and k compared to Cr_2O_3. The Tauc plot for direct bandgap absorption, plotted in Fig. 5(b) as $(\alpha h\nu)^{1/r}$ vs $h\nu$ with $1/r = 2$ and the absorption coefficient α calculated as $\alpha = 4\pi k/\lambda$, indicates that the estimated bandgap for Ti-doped Cr_2O_3 occurs at a somewhat higher energy (3.49 eV) than the bandgap of Cr_2O_3 (3.27 eV). The additional intensity around 3 eV photon energy, apparent in k for Ti-doped Cr_2O_3 compared with pure Cr_2O_3, is manifested in the Tauc plot as a significant absorption tail at approximately 3.0–3.5 eV. This absorption tail does not exhibit a linear region in Fig. 5(b), nor does it exhibit clear linear behavior when plotted with $1/r = 1/2$ (indirect bandgap).

The XPS valence band (VB) spectra for several Ti concentrations, as well as pure Cr_2O_3, are presented in the inset to Fig. 5(b). The spectra have been normalized to the feature at the

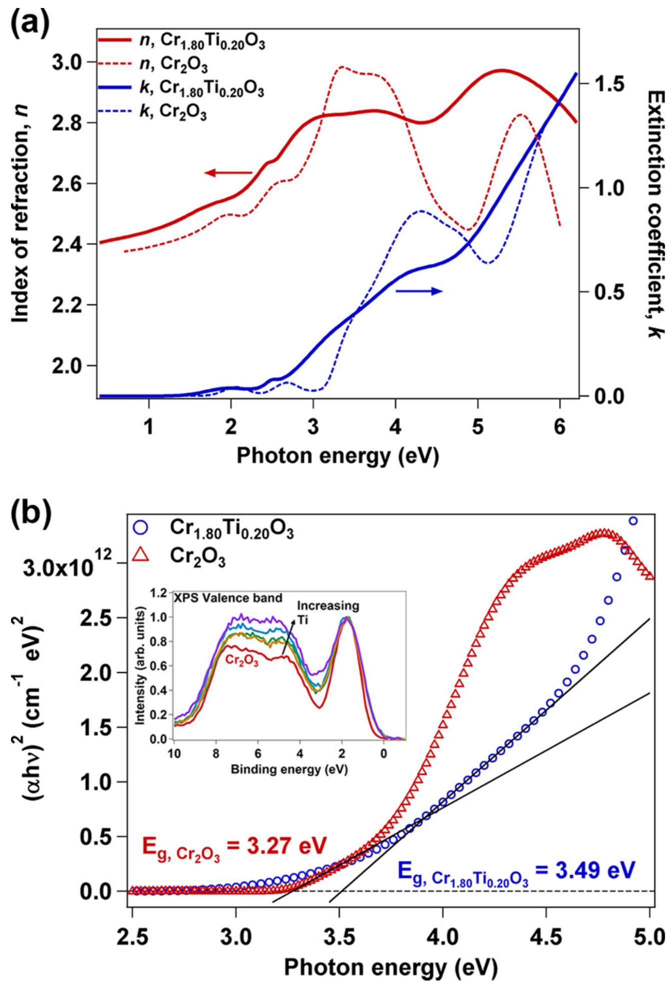

FIG. 5. (a) Index of refraction (n, left axis) and extinction coefficient (k, right axis) from fitting of spectroscopic ellipsometry data for 4900 Å Ti-doped Cr_2O_3 and 4400 Å pure Cr_2O_3. (b) Tauc plot of absorption coefficient to determine direct bandgap values. Inset: *In situ* XPS valence band spectra of pure and Ti-doped Cr_2O_3 films. Spectra have been normalized to the Cr $3d$ feature at the top of the valence band.

top of the VB. This peak derives from occupied Cr $3d\ e_g$ states, and thus as the fraction of Ti increases, this peak diminishes relative to the M$3d$–O$2p$ band (M = Cr,Ti). Close inspection of the leading edge of the VB (near BE = 0 eV) reveals that, while Ti doping slightly broadens the edge, the degree of broadening does not scale with Ti concentration; thus, Ti doping does not add states at the top of the VB. This confirms DFT results [25] (as will also be seen in Fig. 7) that predicted no change to the valence band of Cr_2O_3 with Ti doping.

Room temperature resistance measurements as a function of distance between electrodes (transmission line measurements) were made on the 4900 Å thick $Cr_{1.80}Ti_{0.20}O_3/Al_2O_3(0001)$ sample. As shown in Fig. 6, a linear dependence of resistance on electrode spacing is observed. The sheet resistance of the Ti-doped Cr_2O_3 film, R_s, was calculated from $R = 2R_c + R_s(d/l)$, where R is the slope of the least squares best fit of the data, the intercept is equal to twice the contact resistance R_c, d is the distance between gold electrodes, and l is the length of the electrode (1 mm). An average over three sets of electrodes

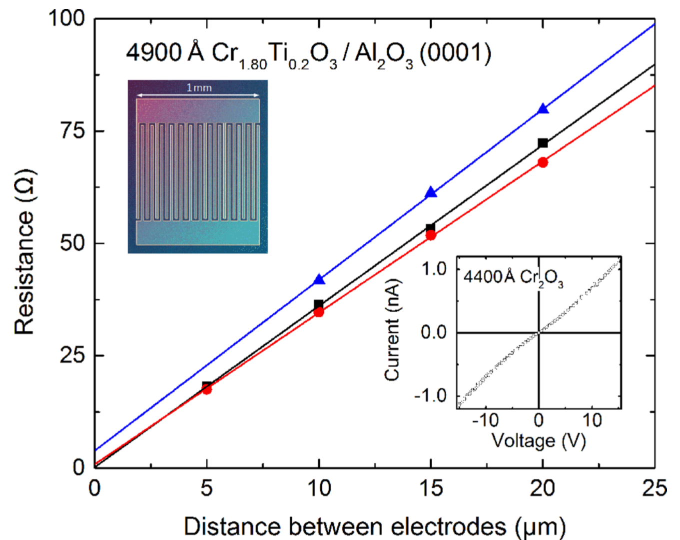

FIG. 6. Resistance as a function of distance between electrodes (transmission line measurements) for three sets of electrodes on the 4900 Å thick $Cr_{1.80}Ti_{0.20}O_3$ film. Sheet resistance is proportional to the slope of the least squares fit (solid line) of the measured resistances (symbols). Top inset: Optical micrograph of interdigitated electrode structure with 7 μm spacing. Bottom inset: Two-terminal I-V data collected with interdigitated electrode structure using 7 μm electrode spacing on 4400 Å thick pure Cr_2O_3 film.

produces a sheet resistance (R_s) of 3.6 ± 0.2 GΩ/□. The film resistivity, neglecting any contribution from the insulating Al_2O_3 substrate, is given by $\rho = R_s \times t$, where t is film thickness. From this, the film resistivity is calculated to be 1.8×10^6 Ω cm. As confirmation that the measured resistance corresponds to bulk resistivity, not surface or interface effects, a thin (500 Å thick) $Cr_{1.84}Ti_{0.16}O_3/Al_2O_3(0001)$ sample was also measured, and a sheet resistance of 62 ± 2 GΩ/□ was found. This corresponds to a resistivity, 3.6×10^6 Ω cm, similar to the thick film, which corroborates the assignment of resistivity as an intrinsic bulk property of Ti-doped Cr_2O_3. For comparison, resistance measurements were made on the 4400 Å thick pure Cr_2O_3 thin film using interdigitated electrode structures with 7 μm electrode spacing. The resulting I-V data are shown in the inset to Fig. 6, and the sheet resistance calculated from this data is estimated to be 105 TΩ/□. This corresponds to a resistivity of approximately 5×10^{10} Ω cm, which is four orders of magnitude larger than that of Ti-doped Cr_2O_3. The sample resistivities of both doped and pure Cr_2O_3 are too high to reliably measure Hall voltages or Seebeck coefficients, precluding determination of the carrier type of either pure or Ti-doped Cr_2O_3.

C. Thermodynamic stability of defects in $Cr_{2-x}Ti_xO_3$

Insights into both the crystalline structure and electronic properties of Ti-doped Cr_2O_3 are gained by performing DFT calculations. A 60-atom supercell ($Cr_{24}O_{36}$) was optimized with respect to the fractional coordinates and lattice parameters using the PBEsol functional. Although PBEsol typically reproduces experimental lattice parameters well [31], in the case of Cr_2O_3 an unexpectedly large lattice parameter deviation from the experimental values (up to 2.4%) was

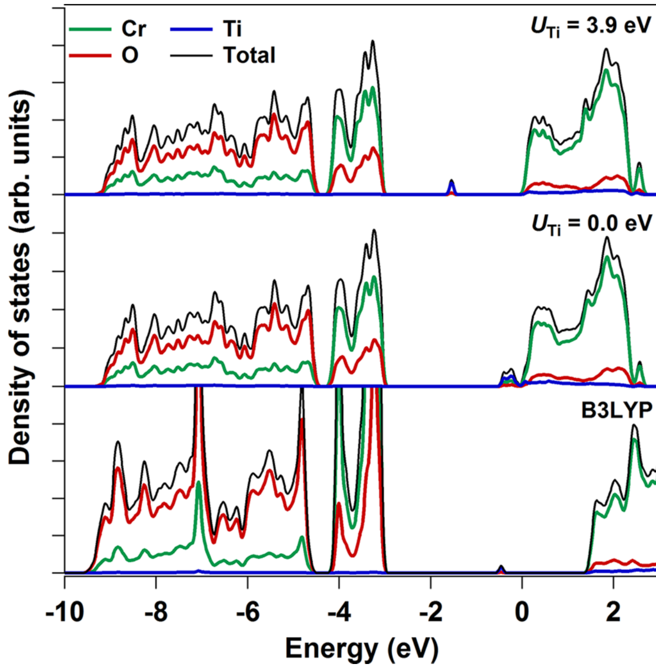

FIG. 7. Partial one-electron densities of states (PDOS) for $Cr_{23}Ti_1O_{36}$ calculated with PBEsol + U with a Hubbard U parameter of $U_{Cr} = 3.9$ eV; $U_{Ti} = 3.9$ eV (top) and $U_{Ti} = 0.0$ eV (middle), as well as (bottom) B3LYP hybrid functionals. All PDOS have been broadened by a Gaussian of FWHM = 0.1 eV.

observed. To correct the lattice parameters, a Hubbard U parameter was introduced. A value of $U = 3.9$ eV was found to correct the in-plane (a) lattice parameter of pure Cr_2O_3 to nearly the experimental value, but no value of U was able to exactly reproduce the experimental c lattice parameter. Thus, $U = 3.9$ eV was utilized for Cr in the calculations, which resulted in lattice parameters of $a = 4.959$ Å and $c = 13.609$ Å. This U value also provided a good approximation of the electronic structure of pure Cr_2O_3; the calculated bandgap of 3.16 eV is reasonably close to the experimental value of 3.3 eV. In contrast, a value of $U = 0$ applied to Ti in a supercell of rutile TiO_2 was found to best reproduce the experimental lattice parameters.

The one-electron densities of states (DOS) and projected DOS calculated for $Cr_{23}Ti_1O_{36}$ (not compensated by V_{Cr} or O_i) with a Hubbard parameter of $U = 3.9$ eV applied to Cr only or Cr and Ti are shown in Fig. 7, together with the DOS calculated using the hybrid B3LYP density functional [49,50]. In all cases, the first Ti^{3+} $3d$ state appears in the Cr_2O_3 bandgap. When $U_{Ti} = 3.9$ eV is applied to the Ti $3d$ states, they appear near midgap, whereas for $U_{Ti} = 0$ the Ti $3d$ states appear near the conduction band minimum (CBM). With the hybrid B3LYP functional, the experimental bandgap of Cr_2O_3 is well approximated, and the Ti^{3+} state is located near midgap. Since $U_{Ti} = 0$ places the Ti^{3+} $3d$ state at the same distance from the top of the VB as does the hybrid calculation, the results presented below used $U_{Ti} = 0$ and $U_{Cr} = 3.9$ eV. In accordance with the XPS valence band results in Fig. 5(b), the partial density of states (PDOS) for all calculations confirms that there is little contribution from Ti in the Cr_2O_3 valence band.

To investigate the energetics, structure, and electronic properties of Ti substitution in Cr_2O_3, supercells of $Cr_{24-m-n}Ti_mO_{36+k}$ were generated for $0 \leqslant m \leqslant 3$, $n = 0$ or 1, and $k = 0$ or 1. Cr vacancies have been hypothesized to dominate in Ti-doped Cr_2O_3 [22], although Cr_2O_3 is known to accommodate excess oxygen [14]. Thus, both Cr vacancies and oxygen interstitials were considered as charge-compensating defects in the calculations. The thermodynamic stability of the most stable configuration of each defect structure relative to both an O_2 molecule and two O atoms, as a function of oxygen activity (the oxygen chemical potential, $\Delta\mu_O$), are shown in Figs. 8(a) and 8(b), respectively. Without Ti doping ($m = 0$, $n = 0$), an additional O atom ($k = 1$) was found to bind to a lattice O^{2-} anion, forming a peroxy-like O_2^{2-} molecular ion. This structure is thermodynamically preferred if pure $Cr_2O_3(m = n = k = 0)$ reacts with oxygen atoms present in the activated oxygen flow. In Ti-doped Cr_2O_3, however, when one or two Ti cations are substituted in the supercell ($m = 1$ or 2, $k = 1$), the additional oxygen instead adopts an interstitial configuration (O^{2-}) by bonding to a Ti cation; the formal charge of the Ti cation becomes +4. If $m = 1$ (one Ti species per supercell), a neighboring Cr cation also experiences a formal charge increase from +3 to +4; however, if $m = 2$ (two Ti species in the supercell), interstitial oxygen preferentially oxidizes both Ti^{3+} to Ti^{4+} instead. Likewise, inclusion of V_{Cr} in the supercell preferentially oxidizes Ti to Ti^{4+}; if fewer than three Ti are present, one or two holes are introduced at the top of the VB to maintain overall charge neutrality. The formation of V_{Cr} is more energetically favorable than the incorporation of oxygen interstitials at lower oxygen activity. Conversely, at higher oxygen activity, oxygen interstitials become somewhat more favorable. These trends hold qualitatively for a range of U parameters explored (2.0–4.4 eV).

Figure 8(c) plots the on-site potential at the Ti dopant cation for selected geometric configurations of $2Ti_{Cr} + V_{Cr}$ and $2Ti_{Cr} + O_i$ calculated above, as well as $2Ti_{Cr}$ without compensating defects, within the 60-atom supercell containing 24 cation sites. It can be noted that there is a broad distribution of potentials for both defect compensation mechanisms. For both $2Ti + V_{Cr}$ and $2Ti + O_i$, the more energetically favorable defect configurations (darker symbol colors) exhibit a less negative on-site potential, while less favorable configurations (lighter symbol colors) are clustered at a somewhat more negative on-site potential. Configurations which result in Ti^{3+} are tightly clustered at an on-site potential which is less negative than the Ti^{4+} potentials. To visualize the effect of these configurations on the experimental Ti $2p$ core level measured by XPS, distributions of the Ti on-site electrostatic potential were constructed by weighing the contribution of each configuration with the corresponding Boltzmann factor and broadening them with Gaussian functions of FWHM = 0.25 eV. The sum of the weighted and broadened potentials for each defect type are presented in Fig. 8(d). For each defect type, the on-site potential for the O1s core level was shifted to align with that for uncompensated Ti^{3+} in Cr_2O_3. The same shifts were applied to the Ti $2p$ on-site potentials in Figs. 8(b) and 8(c); this is analogous to the shifts applied to the XPS data in Fig. 3 which aligned the O1s core level peaks. In Fig. 8(d), $2Ti^{4+} + O_i$ exhibits a broader distribution than

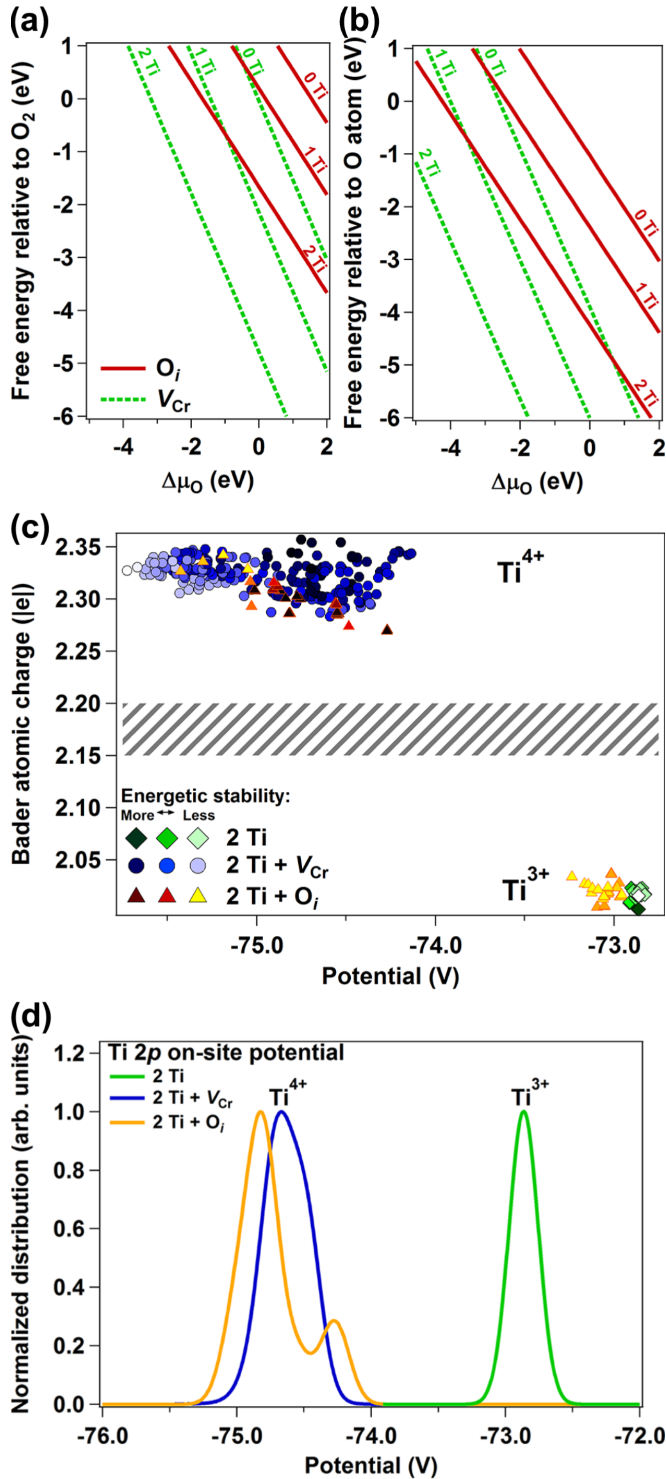

FIG. 8. Calculated defect formation energies as a function of oxygen activity ($\Delta\mu_O$), with respect to the O_2 molecule (a) and two O atoms (b). Results for $m = 0,1$ ($x = 0.042$), and 2 (0.083) Ti dopants are shown. (c) Calculated on-site potential of Ti dopants as a function of atomic (Bader) charge, which is related to the valence charge state of the Ti dopant. Lighter colored symbols represent less energetically favorable defect configurations. (d) Boltzmann distribution of on-site electrostatic potentials, broadened with Gaussians of FWHM = 0.25 eV.

TABLE I. Distance from Cr or Ti to nearest-neighbor oxygens in the first octahedral coordination sphere, as predicted from *ab initio* (DFT) simulations of supercells with various dopant and defect configurations. In all cases, the values are for the lowest energy configuration and are averaged over the three shortest or longest octahedral bonds; the error was taken as the standard deviation of this average. Results from supercells with $m = 1 (x = 0.042)$, 2 (0.083), and 3 (0.125) Ti dopants were averaged for each configuration (except for Cr^{3+}, taken from a pure Cr_2O_3 cell). The difference between average long and short bond lengths is given as Δd.

Configuration	d_{short}(Å)	d_{long}(Å)	Δd(Å)
Cr^{3+}	1.966 ± 0.0003	2.015 ± 0.0004	0.049
Ti^{3+}	1.966 ± 0.02	2.071 ± 0.03	0.105
$Ti^{4+} + O_i$	1.960 ± 0.06	2.134 ± 0.07	0.173
$Ti^{4+} + V_{Cr}$	1.900 ± 0.08	2.062 ± 0.10	0.162

does $2Ti^{4+} + V_{Cr}$, with a majority of the additional intensity present on the left side of the Ti^{4+} distribution. Thus, intensity arising from the presence of $Ti^{4+} + O_i$ is expected to appear at higher BE than that from $Ti + V_{Cr}$ in the experimental Ti 2p XPS spectra.

Average M-O bond lengths from MO_6 octahedra (M = Cr, Ti) corresponding to the most stable configurations of the structures discussed above are given in Table I. The two values for the nearest-neighbor Cr-O bond lengths match reasonably well with the experimental values for the distorted MO_6 octahedra of corundum Cr_2O_3 ($d_{short} = 1.964$ Å and $d_{long} = 2.013$ Å). Substitution of Ti for Cr further distorts the octahedral MO_6. The ionic radius of Ti^{3+}(0.67 Å) is larger than that of Cr^{3+}(0.615 Å), and thus the observed expansion of the $Ti^{3+}O_6$ octahedra, indicated by an increase in d_{long}, is to be expected. A stronger distortion occurs when Ti^{4+} is surrounded by $O_6 + O_i$ in the corundum lattice. When present, interstitial oxygen was included in the bond length calculations. Despite the slightly smaller ionic radius of Ti^{4+} (0.605 Å) than Cr^{3+}, a marked expansion of the $Ti^{4+}O_6$ octahedra is observed, primarily due to an increase in d_{long}. In contrast, the $Ti^{4+}O_6$ octahedra contracts when a Cr vacancy (V_{Cr}), not O_i, forms to maintain charge neutrality. In this case, the distortion results in a significantly reduced d_{short} bond length. To quantify the degree of octahedral distortion in these configurations in an experimentally accessible manner, Table I also lists the difference between the average "long" and "short" M-O bond lengths as Δd. No significant dependence of d_{long} and d_{short} values on Ti concentration was observed.

IV. DISCUSSION

The electrical transport properties of pure Cr_2O_3 at lower temperatures (<1000 °C) have not been well established because the intrinsic conductivity is extremely low, and the carrier concentration is typically dominated by fixed-valence extrinsic defects [21,22]. The high sample resistivity measured here for a very pure Cr_2O_3 thin film, $\rho = 1.5 \times 10^9\ \Omega$ cm, represents the best lower bound estimate to date of the intrinsic transport properties of Cr_2O_3 at room temperature. This resistivity value is considered a lower bound since the adsorbed water film present on the film surface under

ambient conditions may also contribute to the measured conduction.

The spectroscopic data confirm that Ti substitutes in the Cr_2O_3 lattice as Ti^{4+}, but it is clear from the transport measurements that the films are highly resistive. The transport properties of the thick $Cr_{1.80}Ti_{0.20}O_3$ film can be estimated from the resistivity calculated from Fig. 6 ($3.6 \times 10^6\ \Omega\,cm$). Resistivity is related to the carrier concentration and mobility through the relation $\rho = 1/(ne\mu_e + pe\mu_h)$, where e is the electron charge, n and p are the electron and hole concentrations, respectively, and μ_e and μ_h are the electron and hole mobilities, respectively. Resistivity measurements alone cannot determine the electron concentration and mobility, only their product. However, two limiting cases can be assumed which provide bounds on the mobility and free carrier concentration. First, if it is assumed that the hole concentration is negligible ($p = 0$), and further that the electron mobility (μ_e) is governed by polaron hopping and has a similar value as for p-type polarons in Mg-doped Cr_2O_3, $1 \times 10^{-4}\ cm^2/Vs$ [14], the electron concentration n can be estimated as $3.6 \times 10^{16}\ cm^{-3}$. This carrier concentration is four orders of magnitude less than the number of Ti^{4+} dopants in the film ($\sim 4 \times 10^{20}\ cm^{-3}$). The small but real effect of adding Ti^{4+} to Cr_2O_3 is confirmed by a similar calculation using the measured resistivity of pure Cr_2O_3, which results in an estimated electron concentration on the order of $10^{12}\ cm^{-3}$. Alternatively, it can be assumed that, as an upper bound, each Ti^{4+} contributes a free carrier, and the measured resistivity is governed by the mobility of these carriers. Assuming a free electron concentration of $4 \times 10^{20}\ cm^{-3}$, a lower bound on the mobility of $9 \times 10^{-9}\ cm^2/Vs$ is calculated. Although the resistivity data alone cannot distinguish between these two limiting cases, the structural evidence of defect compensation by V_{Cr} and/or O_i indicates that the transport properties are governed by a lower carrier concentration and higher carrier mobility.

This contradicts an earlier theoretical prediction [25] and differs markedly from the reasonably high conduction observed in Ti^{4+}-doped Fe_2O_3, where $\sim 1 \times 10^{20}\ cm^{-3}$ electrons, which exhibited hopping conductivity with a mobility of $\sim 0.2\ cm^2/V\,s$, were found by Hall measurements for a similar Ti doping concentration [18]. The highly resistive behavior of Ti-doped Cr_2O_3 can be qualitatively understood from the DFT results presented above: both V_{Cr} and O_i are thermodynamically favored over Ti^{4+}+ free e^-. Indirect evidence of defect compensation by oxygen interstitials and/or Cr vacancies is observed in the local structure around the Ti dopants, as probed by EXAFS. In Fig. 2(b), strong octahedral distortion is observed for the Ti-doped Cr_2O_3 films. This distortion can be qualitatively correlated to Δd in Table I. Very similar values of Δd are calculated for the $Ti^{4+} + O_i$ complex compared with $Ti^{4+} + V_{Cr}$, which are not significant enough to allow us to distinguish between V_{Cr} and O_i in the EXAFS data. However, the reduced d_{short} bond length for $Ti^{4+} + V_{Cr}$, combined with a slightly expanded d_{long}, match very well to the octahedral distortion presented in Fig. 2(b); for $Cr_{1.84}Ti_{0.16}O_3$ deposited with the oxygen plasma, the predicted bond lengths match the EXAFS data quantitatively. Overall, the dominant role of V_{Cr} in compensating Ti^{4+} dopants is apparent, although the role of O_i cannot be ruled out, given the similar Δd values in Table I.

Further evidence of the localized defect compensation mechanisms intrinsic to Ti-doped Cr_2O_3 is revealed by the Ti $2p$ core level XPS data presented in Fig. 3. Despite the confirmation from XANES (Fig. 4) that the Ti dopants are present as exclusively (or nearly exclusively) Ti^{4+}, the Ti $2p$ core level spectra in Fig. 3(b) are extremely broad. The FWHM of the Ti $2p$ peak exhibits a monotonic dependence on the Ti dopant concentration, with the broadest peaks associated with the lowest Ti concentrations. At intermediate and higher Ti concentrations ($x > \sim 0.1$), the broad shape of the Ti $2p$ core level qualitatively correlates with the distribution of on-site potentials calculated for various configurations of $Ti^{4+} + V_{Cr}$ in Fig. 8(d). As the Ti concentration increases, the probability of three Ti dopants incorporating in the Cr_2O_3 lattice in close proximity to each other also increases, leading to favorable $Ti^{4+} + V_{Cr}$ configurations and thus narrowing the distribution of Ti $2p$ on-site potentials. Note, however, that the broad distribution of on-site potentials (even for favorable configurations) indicates that this peak will never reach the very narrow FWHM associated with Ti^{4+} in TiO_2. Deposition at very low Ti concentrations results in particularly broad Ti $2p$ peaks, which are shifted to higher BE [Fig. 3(b)]. We propose that the increased peak broadening and peak shift are associated with the fact that, at low Ti concentrations where Ti dopants are widely spaced, a fraction of $Ti^{4+} + O_i$ forms in addition to less favorable $Ti^{4+} + V_{Cr}$ configurations. As shown by the calculated on-site potentials in Fig. 8(d), the presence of $Ti^{4+} + O_i$ is expected to both broaden the Ti $2p$ core level peak and add increased spectral intensity to higher BE.

The complex defect structure of Ti-doped Cr_2O_3 revealed here, suggesting a significant Ti doping concentration dependence, provides insights beyond the more simplistic view of previous papers [10,11,20,22,43]. This dependence is not necessarily unique to OPA-MBE deposition. For example, whether activated oxygen from the plasma is utilized during deposition (at a similar oxygen background pressure) does not appear to significantly alter the formation of O_i versus V_{Cr} as compensating defects. This is illustrated in Fig. 3(b), where the Ti $2p$ peak width and position of $x = 0.12$ films deposited at 2×10^{-5} Torr with and without the oxygen plasma, exhibit reasonably similar values. Likewise, the Ti-O nearest-neighbor bond distances exhibit stronger than expected distortion for Ti-doped Cr_2O_3 films deposited with ($x = 0.16$) and without ($x = 0.14$) the oxygen plasma. Only when the O_2 pressure is reduced significantly (8×10^{-7} Torr) does the Ti $2p$ peak shift toward Ti^{3+} [Fig. 3(b)], is some evidence of Ti^{3+} observed in the XANES absorption edge position (Fig. 4), and does the distortion of the Ti octahedral environment become much less pronounced [Fig. 2(b)]. This is associated with concurrent roughening of the Ti-doped Cr_2O_3 film and increased crystalline disorder.

The different behavior of Ti^{4+} dopants in Cr_2O_3 versus Fe_2O_3 can be understood from differences in their band structure. As illustrated for Ti-doped Cr_2O_3 by the hybrid functional (B3LYP) PDOS plots in Fig. 7, the Ti^{3+} $3d$ states lie near midgap, separated from the CBM. These Ti $3d$ states can be removed from the gap by ionizing Ti^{3+} to Ti^{4+}, as observed experimentally. To transfer an electron from Ti^{3+} to the conduction band is energetically costly (estimated as ~ 1.8 eV from the hybrid PDOS in Fig. 7), and from the experimental

results indicating the lack of carriers in the conduction band, we conclude that the energy cost to form V_{Cr} and/or O_i is significantly less. This is corroborated by the formation energies presented in Figs. 8(a) and 8(b), which predict an energy gain to form V_{Cr} at most oxygen activities and O_i at high oxygen activity. Fe_2O_3, in contrast, possesses a bandgap of only 2.1 eV [3]. Assuming a similar distance between the valence band and the midgap Ti^{3+} states as that in Cr_2O_3 ($\sim$2.5 eV from the hybrid calculation), in Fe_2O_3 the Ti 3d states are expected to lie at or above the CBM. Indeed, Ti 3d states at the CBM were observed in a previous simulation of Ti-doped Fe_2O_3 using B3LYP hybrid functionals [16]. Electron transfer from Ti^{3+} to the CBM would then be energetically favorable compared with defect formation. This renders Ti-doped Fe_2O_3 conductive, exhibiting shallow polaron-like conductivity with reasonable carrier mobility [18]. Ti-doped Cr_2O_3, in contrast, exhibits only very weak conductivity resulting from charge hopping between defect states deep in the gap with extremely low carrier mobility. It should be noted, however, that previous experimental work on Ti-doped Fe_2O_3 showed that, if the oxygen activity is increased by decreasing the thin film deposition rate at fixed oxygen pressure, the films become highly resistive. This observation is consistent with the formation of compensating V_{Fe} or O_i defects at higher oxygen chemical potentials, analogous to Ti-doped Cr_2O_3 [see Figs. 8(a) and 8(b)].

As discussed above, earlier studies on the transport properties of bulk Ti-doped Cr_2O_3 monoliths at elevated temperature (1000 °C) have produced conflicting results: Holt and Kofstad [20] observed a crossover from n-type to p-type conductivity at high oxygen activity. However, Atkinson *et al.* [22] found that, for a higher Ti dopant concentration, no crossover occurs; the material remains n-type over all oxygen activities. This disagreement may arise from the Ti concentration dependence of the defect compensation mechanisms that we have observed. At high Ti concentrations such as those investigated by Atkinson *et al.* [22], V_{Cr} is the dominant compensating defect. As the oxygen activity (partial pressure of oxygen in equilibrium with the Ti-doped Cr_2O_3 sample) is varied, the slow self-diffusion kinetics [51] of cations in Cr_2O_3 render the concentration and configuration of V_{Cr} nearly fixed. In this scenario, n-type conductivity arises from hopping between deep defect states, as discussed above for the Ti-doped Cr_2O_3 thin films. However, at low Ti concentrations such as those employed by Holt and Kofstad, the defect compensation mechanisms are hindered by the wide spacing between Ti dopants; less energetically favorable V_{Cr} configurations, as well as O_i configurations, may form. At low oxygen activity, O_i removal from the lattice may be facile, resulting in uncompensated Ti^{4+} which contribute to the n-type conductivity. At high oxygen activity, however, the opposite may occur, and an excess of O_i in the lattice will result in V_{Cr} which are no longer compensated by Ti dopants. Uncompensated V_{Cr} introduces holes into the Cr_2O_3 valence band which could lead to the p-type conductivity observed at low Ti concentrations.

V. CONCLUSIONS

Epitaxial thin films of $Cr_{2-x}Ti_xO_3$ were deposited by OPA-MBE to investigate the structural and electronic effects of Ti doping. Ti dopants were found to incorporate as Ti^{4+} under most deposition conditions; even with the lowest O_2 partial pressure explored, 8×10^{-7} Torr O_2, Ti was incorporated primarily as Ti^{4+} despite the observed structural disorder and surface roughening. In contrast to Ti^{4+} doping of Fe_2O_3, which leads to reasonable values of n-type conductivity, $Cr_{2-x}Ti_xO_3$ thin films were found to be highly resistive. Detailed analysis of the octahedral distortion around the Ti dopant and comparison to relaxed supercells with various types of defect compensation led us to conclude that Ti^{4+} is compensated by O_i and/or V_{Cr}. While the difference in octahedral distortion is not large enough to distinguish between the two, differences in the calculated on-site electrostatic potential of Ti dopants with O_i versus V_{Cr} are clearly distinguishable. These differences are consistent with the broadening of the Ti 2p core level peak observed by XPS. Higher Ti^{4+} dopant concentrations were found to induce primarily V_{Cr} as compensating defects, while very low dopant concentrations appear to exhibit compensation by O_i in addition to less energetically favorable configurations of V_{Cr}. These differences in defect formation with Ti doping level may explain the discrepancy in the literature [20,22], in which p-type conductivity was observed for very low Ti concentrations at elevated temperature and high oxygen activity, but at higher Ti concentrations, n-type conductivity was observed under the same measurement conditions. These insights will inform future studies to exploit the wide variety of electronic and magnetic properties of corundum structure oxides.

ACKNOWLEDGMENTS

The authors are grateful to Vic Henrich for providing the synthetic Ti_2O_3 single crystal. T.C.K., P.V.S., and S.A.C. performed sample synthesis, characterization, data analysis, and theoretical simulations with support from the U.S. Department of Energy (DOE), Office of Science, Office of Basic Energy Sciences (BES), Division of Materials Sciences and Engineering, under Award No. 10122. A.P., C.T., and O.B. performed electrical transport measurements and associated data analysis and acknowledge W. Seidel and B. Drescher for processing. A portion of this work was performed using EMSL, a national scientific user facility sponsored by the U.S. DOE's Office of Biological and Environmental Research and located at the Pacific Northwest National Laboratory (PNNL). PNNL is a multiprogram national laboratory operated for DOE by Battelle under Contract No. DE-AC05-76RL01830. XAS data were collected on an XSD beamline 20-BM of the Advanced Photon Source, a U.S. Department of Energy (DOE) Office of Science User Facility operated for the DOE Office of Science by Argonne National Laboratory under Contract No. DE-AC02-06CH11357.

[1] C. O. A. Olsson and D. Landolt, Electrochim. Acta **48**, 1093 (2003).

[2] F. H. Stott, G. C. Wood, and J. Stringer, Oxid. Met. **44**, 113 (1995).

[3] S. E. Chamberlin, Y. Wang, T. C. Kaspar, A. W. Cohn, D. R. Gamelin, P. V. Sushko, and S. A. Chambers, J. Phys.: Condens. Matter **25**, 392002 (2013).
[4] H. Mashiko, T. Oshima, and A. Ohtomo, Appl. Phys. Lett. **99**, 241904 (2011).
[5] T. C. Kaspar, D. K. Schreiber, S. R. Spurgeon, M. E. McBriarty, G. M. Carroll, D. R. Gamelin, and S. A. Chambers, Adv. Mater. **28**, 1616 (2016).
[6] M. Imada, A. Fujimori, and Y. Tokura, Rev. Mod. Phys. **70**, 1039 (1998).
[7] D. R. Lide, *CRC Handbook of Chemistry and Physics*, 84th ed. (CRC Press, Boca Raton, FL, 2003).
[8] G. T. Rado and V. J. Folen, Phys. Rev. Lett. **7**, 310 (1961).
[9] P. T. Moseley and D. E. Williams, Sens. Actuators B: Chem. **1**, 113 (1990).
[10] G. S. Henshaw, D. H. Dawson, and D. E. Williams, J. Mater. Chem. **5**, 1791 (1995).
[11] D. Niemeyer, D. E. Williams, P. Smith, K. F. E. Pratt, B. Slater, C. R. A. Catlow, and A. M. Stoneham, J. Mater. Chem. **12**, 667 (2002).
[12] J. Du, Y. Q. Wu, and K. L. Choy, Thin Solid Films **497**, 42 (2006).
[13] G. A. Shaw, I. P. Parkin, and D. E. Williams, J. Mater. Chem. **13**, 2957 (2003).
[14] L. Farrell, K. Fleischer, D. Caffrey, D. Mullarkey, E. Norton, and I. V. Shvets, Phys. Rev. B **91**, 125202 (2015).
[15] K. M. Rosso, D. M. A. Smith, and M. Dupuis, J. Chem. Phys. **118**, 6455 (2003).
[16] T. Droubay, K. M. Rosso, S. M. Heald, D. E. McCready, C. M. Wang, and S. A. Chambers, Phys. Rev. B **75**, 104412 (2007).
[17] M. Rioult, H. Magnan, D. Stanescu, and A. Barbier, J. Phys. Chem. C **118**, 3007 (2014).
[18] B. Zhao, T. C. Kaspar, T. C. Droubay, J. McCloy, M. E. Bowden, V. Shutthanandan, S. M. Heald, and S. A. Chambers, Phys. Rev. B **84**, 245325 (2011).
[19] D. Morris, Y. Dou, J. Rebane, C. E. J. Mitchell, R. G. Egdell, D. S. L. Law, A. Vittadini, and M. Casarin, Phys. Rev. B **61**, 13445 (2000).
[20] A. Holt and P. Kofstad, Solid State Ionics **117**, 21 (1999).
[21] A. Holt and P. Kofstad, Solid State Ionics **69**, 137 (1994).
[22] A. Atkinson, M. R. Levy, S. Roche, and R. A. Rudkin, Solid State Ionics **177**, 1767 (2006).
[23] A. Conde-Gallardo, A. Cruz-Orea, O. Zelaya-Angel, and P. Bartolo-Perez, J. Phys. D: Appl. Phys. **41**, 205407 (2008).
[24] V. T. Rangel-Kuoppa and A. Conde-Gallardo, Thin Solid Films **519**, 453 (2010).
[25] F. Maldonado, C. Novillo, and A. Stashans, Chem. Phys. **393**, 148 (2012).
[26] T. C. Kaspar, S. E. Chamberlin, and S. A. Chambers, Surf. Sci. **618**, 159 (2013).
[27] L. Qiao, T. C. Droubay, M. E. Bowden, V. Shutthanandan, T. C. Kaspar, and S. A. Chambers, Appl. Phys. Lett. **99**, 061904 (2011).
[28] S. A. Chambers and T. Droubay, Phys. Rev. B **64**, 075410 (2001).
[29] G. Kresse and D. Joubert, Phys. Rev. B **59**, 1758 (1999).
[30] J. P. Perdew, K. Burke, and M. Ernzerhof, Phys. Rev. Lett. **77**, 3865 (1996).
[31] J. P. Perdew, A. Ruzsinszky, G. I. Csonka, O. A. Vydrov, G. E. Scuseria, L. A. Constantin, X. L. Zhou, and K. Burke, Phys. Rev. Lett. **100**, 136406 (2008).
[32] S. L. Dudarev, G. A. Botton, S. Y. Savrasov, C. J. Humphreys, and A. P. Sutton, Phys. Rev. B **57**, 1505 (1998).
[33] E. Heifets, J. Ho, and B. Merinov, Phys. Rev. B **75**, 155431 (2007).
[34] S. A. Chambers, in *Oxide Surfaces*, edited by D. P. Woodruff (Elsevier, New York, 2001), p. 301.
[35] S. A. Chambers and S. I. Yi, Surf. Sci. **439**, L785 (1999).
[36] Y. Gao, Y. J. Kim, S. A. Chambers, and G. Bai, J. Vac. Sci. Technol. A **15**, 332 (1997).
[37] Y. J. Kim, Y. Gao, and S. A. Chambers, Appl. Surf. Sci. **120**, 250 (1997).
[38] S. Thevuthasan, Y. J. Kim, S. I. Yi, S. A. Chambers, J. Morais, R. Denecke, C. S. Fadley, P. Liu, T. Kendelewicz, and G. E. Brown, Surf. Sci. **425**, 276 (1999).
[39] S. I. Yi, Y. Liang, and S. A. Chambers, J. Vac. Sci. Technol. A **17**, 1737 (1999).
[40] T. C. Kaspar, S. E. Chamberlin, M. E. Bowden, R. Colby, V. Shutthanandan, S. Manandhar, Y. Wang, P. V. Sushko, and S. A. Chambers, J. Phys.: Condens. Matter **26**, 135005 (2014).
[41] S. A. Chambers, Y. Liang, and Y. Gao, Phys. Rev. B **61**, 13223 (2000).
[42] S. E. Chamberlin, T. C. Kaspar, M. E. Bowden, V. Shutthanandan, B. Kabius, S. Heald, D. Keavney, and S. A. Chambers, J. Appl. Phys. **116**, 233702 (2014).
[43] A. N. Blacklocks, A. Atkinson, R. J. Packer, S. L. P. Savin, and A. V. Chadwick, Solid State Ionics **177**, 2939 (2006).
[44] S. A. Chambers, T. Ohsawa, C. M. Wang, I. Lyubinetsky, and J. E. Jaffe, Surf. Sci. **603**, 771 (2009).
[45] S. A. Chambers, S. H. Cheung, V. Shutthanandan, S. Thevuthasan, M. K. Bowman, and A. G. Joly, Chem. Phys. **339**, 27 (2007).
[46] J. Pouilleau, D. Devilliers, H. Groult, and P. Marcus, J. Mater. Sci. **32**, 5645 (1997).
[47] P. M. Kumar, S. Badrinarayanan, and M. Sastry, Thin Solid Films **358**, 122 (2000).
[48] K. E. Smith and V. E. Henrich, Phys. Rev. B **38**, 5965 (1988).
[49] A. D. Becke, J. Chem. Phys. **98**, 5648 (1993).
[50] C. T. Lee, W. T. Yang, and R. G. Parr, Phys. Rev. B **37**, 785 (1988).
[51] A. Holt and P. Kofstad, Solid State Ionics **69**, 127 (1994).